

# Polar coordinate lattice Boltzmann modeling of detonation phenomena

Chuangdong Lin<sup>1</sup>, Aiguo Xu<sup>2‡</sup>, Guangcai Zhang<sup>2</sup> and Yingjun Li<sup>1§</sup>

<sup>1</sup> State Key Laboratory for GeoMechanics and Deep Underground Engineering, China University of Mining and Technology, Beijing 100083, P.R.China

<sup>2</sup> National Key Laboratory of Computational Physics, Institute of Applied Physics and Computational Mathematics, P. O. Box 8009-26, Beijing 100088, P.R.China

**Abstract.** We present a polar coordinate lattice Boltzmann model for the detonation phenomena. In this model the fluid behavior is describe by a finite-difference lattice Boltzmann(FDLB) model in polar coordinates, and the chemical reaction is described by Cochran's rate function. The released chemical energy is naturally coupled with the flow behavior. We introduce an operator-splitting scheme to both the FDLB equation and Cochran's rate function. The temporal evolutions are calculated analytically and the convection terms are solved via the first-order upwind scheme. The model is validated and verified via comparing simulation results with analytical solution of steady detonation. We simulate the detonation phenomena in two cases: implosion and explosion. Finally, we study some non-equilibrium characteristics in the steady detonation procedure. Numerical results show that, the amplitudes of deviations from thermodynamic equilibrium in front of von-Neumann peak are much higher than those behind the peak. At the von Neumann peak, the system is nearly in its thermodynamic equilibrium. By comparing each component of the high-order moments and its value in equilibrium, we draw qualitative information on the actual distribution functions at the two sides of von-Neumann peak. Such observations are helpful for the physical modeling of detonation phenomena from the macroscopic level.

PACS numbers: 47.11.-j, 47.40.-x, 47.70.-n

‡ Corresponding author. E-mail address: Xu\_Aiguo@iapcm.ac.cn

§ Corresponding author. E-mail address: lyj@aphy.iphy.ac.cn

## 1. Introduction

Deflagration and detonation are two kinds of combustion phenomena. The former spreads via thermal conductivity, the latter propagates through detonation wave which is a shock wave with chemical reaction. Given a wide range of application in science and engineering, shock and detonation have always been of great concern in the field of science and technology. The detonation phenomena are widely used in the acceleration of various projectiles, mining technologies, depositing of coating to a surface or cleaning of equipment, etc. Early in 1899 and 1905, Chapman and Jouguet[1, 2] presented CJ theory, respectively. This theory assumes that detonation front is a strong discontinuous plane with chemical reaction which immediately completes as soon as the detonation wave passes. In years of 1940, 1942 and 1943, Zeldovich, Neumann and Doering[3, 4, 5] presented the ZND model, respectively. This model gives an important conclusion that there is von-Neumann-peak at detonation wave front. Reactant is firstly pre-compressed by shock wave where is no chemical reaction. There is a continuous reaction zone after that shock wave. Physical quantities (density, temperature, pressure and velocity) reach maximum values within the reaction zone.

Although detonation has been studied for many years, it remains an active area of research in both theoretical studies and numerical simulations due to its practical importance.[6] For modeling of the detonation phenomena, one challenge is how to treat with the chemical reaction and energy releasing processes coupled with flow behavior. So far, all chemical reaction models[7] are empirical or semi-empirical formulas, such as the Arrhenius kinetics, Cochran's rate function, forest fire burn, two-step model, Lee-Tarver model[8], etc. Selecting appropriate chemical reaction kinetics is very important for describing detonation phenomena under consideration. In this paper, we adopt Cochran's rate function[9] for chemical reaction, which is one of the most physically justifiable models satisfying simulation and experimental results.[10, 11]

During recent 26 years, lattice Boltzmann (LB) method has achieved great success in various fields of fluid dynamics and beyond.[12] LB modeling for combustion phenomena has been an interesting topic in LB field from early days, but the progress was very limited. Because previous studies on LB model were mainly focused on isothermal and incompressible fluid systems. Those models generally can not recover the correct energy equation or describe enough the compressibility in the hydrodynamic limit, which make difficult the modeling of systems with shock and/or detonation. At the same time, those LB models assume that exothermic reaction has no significant effect on fluid field, which also constrains the practical application of the models to most cases of combustion. In recent years, the development of LB models for high speed compressible flows[13, 14, 15, 16, 17, 18, 19, 20, 21, 22, 23, 24, 25] makes possible to simulate systems with shock and detonation. Very recently Yan, Xu, Zhang, et al. proposed a LB model for detonation phenomena in Cartesian coordinates.[26]

For simulating the explosion and implosion behaviors, the polar coordinate LB model is obviously more convenient. In 2011 Watari[27] proposed a finite-difference LB

methods in polar coordinate system. In 2013 we[28] improved the LB model so that it works also for supersonic flows. Within the improved model, the temporal and spatial evolutions are treated with via the operator-splitting scheme. The temporal evolution is calculated analytically and the convection term is solved via a Modified Warming-Beam (MWB) scheme. We propose a polar coordinate LB model for simulating detonation phenomena in this work.

In contrast to traditional methods based on Navier-Stokes description, the LB model has some intrinsic superiority in describing kinetic mechanisms in systems where equilibrium and non-equilibrium behaviors coexist.[12, 13, 26, 28] From the mini-review[13] we are trying to answer the following questions: why some (not all) LB models, which recover Navier-Stokes or Euler equations in the hydrodynamic limit, can also be used to investigate non-equilibrium behavior of the system? How to do measure and investigate these behavior? What can we get from those results? The non-equilibrium behaviors in various complex systems are attracting more attention with time.[13, 26, 28, 29, 30] In the work[26] by Yan, Xu, Zhang, et al., some non-equilibrium behavior around the von Neumann peak are obtained. In a recent work[28], we studied the non-equilibrium characteristics of the system around three kinds of interfaces, the shock wave, the rarefaction wave and the material interface, for two specific cases. We draw qualitative information on the actual distribution function. In this work, we further investigate the macroscopic behavior due to deviating from local thermodynamic equilibrium in the detonation procedure.

The rest of the paper is structured as follows. In section II we first briefly describe polar coordinate LB model for compressible fluid. Section III is for simulation and investigation of detonation phenomena. In section IV we study the non-equilibrium characteristics of the system in the cases with shock and detonation. The actual distribution functions are qualitatively illustrated. Section V gives the conclusion and discussions.

## 2. Polar FDLB model

In a polar coordinate system, the Boltzmann equation with the Bhatnager-Gross-Krook approximation reads,

$$\frac{\partial f_{ki}}{\partial t} + v_{kir} \frac{\partial f_{ki}}{\partial r} + \frac{1}{r} v_{ki\theta} \frac{\partial f_{ki}}{\partial \theta} = -\frac{1}{\tau} [f_{ki} - f_{ki}^{eq}], \quad (1)$$

where  $r$  and  $\theta$  are the radial and azimuthal coordinates, respectively;  $f_{ki}$  and  $f_{ki}^{eq}$  are the discrete and equilibrium distribution function, respectively;  $\tau$  is the relaxation time;  $v_{kir}$  and  $v_{ki\theta}$  are the radial and azimuthal components of the discrete velocity  $\mathbf{v}_{ki}$  which will be defined below.

### 2.1. Outline of DVM by Watari-Tsutahara

The Discrete-Velocity-Model (DVM) used in this work is originally presented by Watari and Tsutahara.[27, 31] It has  $(N_k + 1)$  groups of discrete velocities, and  $N_k = 4$  here.

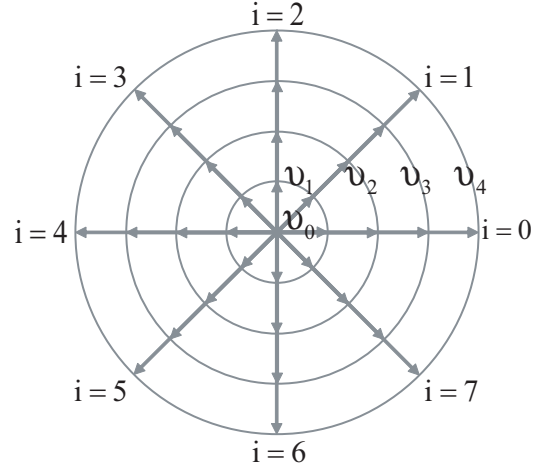


**Figure 1.** Sketch of DVM

The subscript  $k$  indicates the  $k$ -th group of the particle velocities whose speed is  $v_k$ . Each group has  $(N_i + 1)$  components distributed in  $(N_i + 1)$  directions, and  $N_i = 7$  here. Mathematically, the DVM is written as below:

$$\begin{cases} \mathbf{v}_{ki} = v_{kir}\mathbf{e}_r + v_{ki\theta}\mathbf{e}_\theta \\ v_{kir} = v_k \cos\left[\frac{2\pi i}{N_i} - \theta\right] \\ v_{ki\theta} = v_k \sin\left[\frac{2\pi i}{N_i} - \theta\right] \end{cases}, \quad (2)$$

where  $\mathbf{e}_r$  and  $\mathbf{e}_\theta$  are unit vectors,  $k = 0, 1, \dots, N_k$  and  $i = 0, 2, \dots, N_i$ . In this work we choose  $v_0 = 0$ ,  $v_1 = 1.5$ ,  $v_2 = 3.5$ ,  $v_3 = 7.5$ ,  $v_4 = 12.5$ . The sketch of DVM is shown in Fig.1.

The local equilibrium distribution function  $f_{ki}^{eq}$  is calculated in the following way,

$$f_{ki}^{eq} = \rho F_k \left[ \left(1 - \frac{u^2}{2E} + \frac{u^4}{8E^2}\right) + \frac{v_{ki\varepsilon}u_\varepsilon}{E} \left(1 - \frac{u^2}{2E}\right) + \frac{v_{ki\varepsilon}v_{ki\pi}u_\varepsilon u_\pi}{2E^2} \left(1 - \frac{u^2}{2E}\right) \right] \quad (3)$$

$$+ \frac{v_{ki\varepsilon}v_{ki\pi}v_{ki\vartheta}u_\varepsilon u_\pi u_\vartheta}{6E^3} + \frac{v_{ki\varepsilon}v_{ki\pi}v_{ki\vartheta}v_{ki\xi}u_\varepsilon u_\pi u_\vartheta u_\xi}{24E^4} \quad (4)$$

with weighting coefficients

$$F_k = \frac{1}{v_k^2(v_k^2 - v_{k+1}^2)(v_k^2 - v_{k+2}^2)(v_k^2 - v_{k+3}^2)} [B_4 E^4 + B_3(v_{k+1}^2 + v_{k+2}^2 + v_{k+3}^2)E^3 + B_2(v_{k+1}^2 v_{k+2}^2 + v_{k+2}^2 v_{k+3}^2 + v_{k+3}^2 v_{k+1}^2)E^2 + B_1 v_{k+1}^2 v_{k+2}^2 v_{k+3}^2 E], \quad (5)$$

$$F_0 = 1/B_0 - (F_1 + F_2 + F_3 + F_4), \quad (6)$$

$$\{k+l\} = \begin{cases} k+l & \text{for } k+l \leq 4 \\ k+l-4 & \text{for } k+l > 4 \end{cases}, \quad (7)$$

where  $B_0 = 8$ ,  $B_1 = -1/4$ ,  $B_2 = 1$ ,  $B_3 = -6$ ,  $B_4 = 48$ . The local equilibrium distribution function satisfies the following seven relations,

$$\rho = \sum_{ki} f_{ki}^{eq}, \quad (8)$$

$$\rho \mathbf{u} = \sum_{ki} f_{ki}^{eq} \mathbf{v}_{ki}, \quad (9)$$

$$\rho T = \sum_{ki} \frac{1}{2} f_{ki}^{eq} (\mathbf{v}_{ki} - \mathbf{u}) \cdot (\mathbf{v}_{ki} - \mathbf{u}), \quad (10)$$

$$\sum_{ki} f_{ki}^{eq} \mathbf{v}_{ki} \mathbf{v}_{ki} = \rho (E \mathbf{I} + \mathbf{u} \mathbf{u}), \quad (11)$$

$$\sum_{ki} f_{ki}^{eq} \mathbf{v}_{ki} \mathbf{v}_{ki} \mathbf{v}_{ki} = \rho [E (\mathbf{u}_\alpha \mathbf{e}_\beta \mathbf{e}_\gamma \delta_{\beta\gamma} + \mathbf{e}_\alpha \mathbf{u}_\beta \mathbf{e}_\gamma \delta_{\gamma\alpha} + \mathbf{e}_\alpha \mathbf{e}_\beta \mathbf{u}_\gamma \delta_{\alpha\beta}) + \mathbf{u} \mathbf{u} \mathbf{u}], \quad (12)$$

$$\sum_{ki} \frac{1}{2} f_{ki}^{eq} \mathbf{v}_{ki} \cdot \mathbf{v}_{ki} \mathbf{v}_{ki} = \rho (E \mathbf{I} + \mathbf{u} \mathbf{u}), \quad (13)$$

$$\sum_{ki} \frac{1}{2} f_{ki}^{eq} \mathbf{v}_{ki} \cdot \mathbf{v}_{ki} \mathbf{v}_{ki} \mathbf{v}_{ki} = \rho (2E + \frac{1}{2} \mathbf{u} \cdot \mathbf{u}) (E \mathbf{I} + \mathbf{u} \mathbf{u}). \quad (14)$$

Here  $\rho$  is local partial density,  $\mathbf{u}$  ( $= u_r \mathbf{e}_r + u_\theta \mathbf{e}_\theta$ ) is hydrodynamic velocity,  $T$  is temperature,  $P$  ( $= \rho T$ ) is pressure,  $E$  ( $= T/(\gamma - 1)$ ) is internal energy per unit mass,  $\gamma$  ( $= 2$ ) is specific-heat ratio,  $\mathbf{I}$  is unit tensor,  $\mathbf{v}_{ki} \mathbf{v}_{ki}$  ( $\mathbf{u} \mathbf{u}$ ) is a double dyadic,  $\mathbf{v}_{ki} \mathbf{v}_{ki} \mathbf{v}_{ki}$  ( $\mathbf{u} \mathbf{u} \mathbf{u}$ ) is a triple dyadic. With the Chapman-Enskog expansion, the polar coordinate LB model presents the same results as Navier-Stokes equations,

$$\frac{\partial \rho}{\partial t} + \nabla \cdot (\rho \mathbf{u}) = 0, \quad (15)$$

$$\frac{\partial (\rho \mathbf{u})}{\partial t} + \nabla \cdot (P \mathbf{I} + \rho \mathbf{u} \mathbf{u}) + \nabla \cdot [\mu (\nabla \cdot \mathbf{u}) \mathbf{I} - \mu (\nabla \cdot \mathbf{u}) \mathbf{I}] = 0, \quad (16)$$

$$\begin{aligned} & \frac{\partial}{\partial t} (\rho E + \frac{1}{2} \rho u^2) + \nabla \cdot [\rho \mathbf{u} (E + \frac{1}{2} u^2 + \frac{P}{\rho})] \\ & - \nabla \cdot [\kappa' \nabla E + \mu \mathbf{u} \cdot (\nabla \mathbf{u}) - \mu \mathbf{u} (\nabla \cdot \mathbf{u}) + \frac{1}{2} \mu \nabla u^2] = 0, \end{aligned} \quad (17)$$

in the hydrodynamic limit, where  $\mu$  ( $= P\tau$ ) is viscosity coefficient and  $\kappa'$  ( $= 2P\tau$ ) is heat conductivity.

## 2.2. LB evolution equation

The two-dimensional FDLB Eq.(1) can be decomposed into the following one-dimensional form

$$\begin{cases} \frac{\partial f_{ki}}{\partial t} = -\frac{1}{\tau} [f_{ki} - f_{ki}^{eq}] \\ \frac{\partial f_{ki}}{\partial t} + v_{kir} \frac{\partial f_{ki}}{\partial r} = 0 \\ \frac{\partial f_{ki}}{\partial t} + \frac{1}{r} v_{ki\theta} \frac{\partial f_{ki}}{\partial \theta} = 0, \end{cases} \quad (18)$$

via the operator splitting scheme.

The first subequation in Eq.(18) has an analytical solution dynamically as below

$$f_{ki,t}^{t+dt} = \exp(-\frac{dt}{\tau}) [f_{ki}^t - f_{ki}^{eq} + f_{ki}^{eq} \exp(\frac{dt}{\tau})], \quad (19)$$

where  $f_{ki}^t$  is the local distribution function at time  $t$ , and  $f_{ki,t}^{t+dt}$  is the one at time  $t + dt$  corresponding to the first subequation.

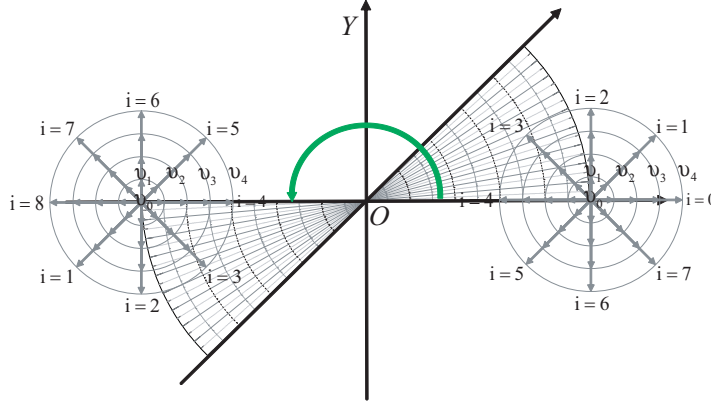


**Figure 2.** Rotation of the distribution functions from the first to the fifth part of physical field in an annular or circular area with period  $N_i$  in circumferential direction.

The last two subequations in Eq.(18) are calculated by using the first order upwind scheme,

$$f_{ki,r}^{t+dt} - f_{ki}^t = \begin{cases} C_r(f_{ki}(i_r, i_\theta) - f_{ki}(i_r - 1, i_\theta)) & \text{for } C_r \geq 0, \\ C_r(f_{ki}(i_r + 1, i_\theta) - f_{ki}(i_r, i_\theta)) & \text{for } C_r < 0, \end{cases} \quad (20)$$

$$f_{ki,\theta}^{t+dt} - f_{ki}^t = \begin{cases} C_\theta(f_{ki}(i_r, i_\theta) - f_{ki}(i_r, i_\theta - 1)) & \text{for } C_\theta \geq 0, \\ C_\theta(f_{ki}(i_r, i_\theta + 1) - f_{ki}(i_r, i_\theta)) & \text{for } C_\theta < 0, \end{cases} \quad (21)$$

where  $C_r = v_{kir} \frac{dt}{dr}$  and  $C_\theta = \frac{1}{r} v_{ki\theta} \frac{dt}{d\theta}$  are Courant-numbers.  $f_{ki,r}^{t+dt}$  and  $f_{ki,\theta}^{t+dt}$  are the solutions correspond to the last two subequations in Eq.(18), respectively.

By composing the solutions of the three subequations in Eq.(18), we get the combined scheme for the LB evolution,

$$f_{ki}^{t+dt} = f_{ki,t}^{t+dt} + (f_{ki,r}^{t+dt} - f_{ki}^t) + (f_{ki,\theta}^{t+dt} - f_{ki}^t). \quad (22)$$

It should be pointed out that the calculation order of splitting scheme in Eq.(18) is not under consideration in Eq.(22). Other calculation methods considering the order can also be adopted. There is a little difference between them, see Appendix.

### 2.3. Boundary conditions

There are two kinds of physical space under consideration in this work. One is an annular area with radii  $R_2 > R_1 > 0$ . The other is a round with radius  $R$ . If the physical field, within either an annular or circular area, is periodic and the period is  $N_i$  in circumferential direction, it can be divided into  $N_i$  parts, where  $N_i$  is just the total number of the directions of discrete velocity in the DVM. Then, we can choose only one part for calculations, i.e., the computational area is given as  $0 < \theta \leq 2\pi/N_i$ . Figure 2 shows the relation between the distribution functions in the first and the fifth part of physical field within a periodic annular or circular area by rotation.

*2.3.1. Radial boundary condition* As for annular area, the total number of radial nodes is given as  $N_r$ , radial increment is  $\Delta r = (R_2 - R_1)/(N_r - 1)$ , and the radius  $r = R_1 + (i_r - 1) \times \Delta r$ , where  $i_r = 1, 2, \dots, N_r$ . The following radial boundary conditions are imposed: inflow (or outflow) condition at inner boundary, outflow (or inflow) condition at outer boundary.

As for circular area, similarly, the number of radial nodes is  $N_r$ , radial increment is  $\Delta r = R/N_r$ , and the radius  $r = (i_r - 1/2) \times \Delta r$ , where  $i_r = 1, 2, \dots, N_r$ . Around the center, the values on the ghost nodes ( $i_r = -1, 0$ ) are calculated via

$$\begin{cases} f(0, i_\theta, k, i) &= f(1, i_\theta, k, \text{mod}(i + N_i/2, N_i)), \\ f(-1, i_\theta, k, i) &= f(2, i_\theta, k, \text{mod}(i + N_i/2, N_i)). \end{cases} \quad (23)$$

The distribution functions on ghost nodes ( $i_r = N_r + 1, N_r + 2$ ) beyond the outer side of the circular area can be given in the same way as those at the outer boundary in an annular area above.

*2.3.2. Azimuthal boundary condition* The total number of azimuthal nodes is  $N_\theta$ , azimuthal increment is  $\Delta\theta = 2\pi/(N_i N_\theta)$ , and the angle  $\theta = i_\theta \times \Delta\theta$ , where  $i_\theta = 1, 2, \dots, N_\theta$ . The distribution functions on ghost nodes ( $i_\theta = -1, 0, N_\theta + 1, N_\theta + 2$ ) are computed via

$$f(i_r, i_\theta, k, i) = \begin{cases} f(i_r, N_\theta + i_\theta, k, \text{mod}(i + 1, N_i)) & \text{for } i_\theta \leq 0, \\ f(i_r, i_\theta - N_\theta, k, \text{mod}(i - 1 + N_i, N_i)) & \text{for } i_\theta > N_\theta. \end{cases} \quad (24)$$

### 3. Detonation

Detonation is complex progress with mutually influence between fluid dynamics and chemical reaction kinetics. It involves a supersonic exothermic front accelerating through a medium that eventually drives a shock front propagating directly in front of it. As detonation wave sweeps over media, the density, temperature and pressure increase immediately.

#### 3.1. Hugoniot relations for detonation

Theoretically, physical quantities in the progress of detonation satisfy the following Hugoniot relations,

$$\begin{cases} \rho_H(u - D) &= \rho_0(u_0 - D), \\ P_H - P_0 &= \rho_0(D - u_0)(u - u_0), \\ E_H - E_0 &= \frac{1}{2}(P_H + P_0) \left( \frac{1}{\rho_0} - \frac{1}{\rho_H} \right) + Q. \end{cases} \quad (25)$$

Here the subscript 0 indicates pre-shocked regions filled with explosive, the subscript  $H$  indicates the shocked region filled with explosive products.  $Q (= \lambda q)$  is released chemical energy of reactant per mass in the progress of reaction,  $q$  is the released chemical energy of reactant per mass in complete reaction,  $\lambda (= \rho_{re}/\rho)$  is a parameter for chemical reaction progress or the fraction of reacted reactant, and  $\rho_{re}$  is the density

of reacted reactant. If  $q = 0$ , then Eq.(25) reduces to the Hugoniot relations of shock wave.  $D$  is the velocity of detonation wave, which satisfies the following rule when it propagates stably,

$$\frac{P_H - P_0}{v_0 - v_H} = \left(-\frac{dP}{dv}\right)_S = \frac{\gamma P_H}{v_H}, \quad (26)$$

where  $v_0 = 1/\rho_0$ ,  $v_H = 1/\rho_H$ ,  $v = 1/\rho$ , the subscript  $S$  indicates isentropic line. Equation (26) corresponds to the relation  $D = C_H + u_H$ , and  $C_H$  is sound velocity. If the explosive and its products are ideal gas which satisfy the relation  $E = Pv(\gamma - 1)$ , we get the following analytic solutions

$$\begin{cases} D = \sqrt{(\gamma^2 - 1)Q/2 + C_0^2} + \sqrt{(\gamma^2 - 1)Q/2} \\ P_H = P_0 + \rho_0(D^2 - C_0^2)/(\gamma + 1) \\ v_H = v_0 - v_0(1 - C_0^2/D^2)/(\gamma + 1) \\ u_H = D(1 - C_0^2/D^2)/(\gamma + 1) \\ T_H = (\gamma D^2 + C_0^2)^2[\gamma(\gamma + 1)D^2]^{-1}. \end{cases} \quad (27)$$

### 3.2. Cochran's rate function

It's very important to select an appropriate chemical reaction kinetic to describe the detonation phenomena under consideration. The reaction model decides the simulation of detonation in the whole progress, including the initiation, development and propagation. So far, most of the chemical reaction kinetics are phenomenological models. In 1979 Cochran and Chan[9] presented a function as below

$$\frac{d\lambda}{dt} = \omega_1 P^m (1 - \lambda) + \omega_2 P^n \lambda (1 - \lambda). \quad (28)$$

The right side of eq.(28) is composed of two terms: the former is the hot formation term mainly describing the formation and subsequent growth of the hot spots, the latter is the growth term mainly describing the growth of the reaction.  $P^m$  and  $P^n$  describe the dependence on the local pressure. The parameters  $\omega_1$ ,  $\omega_2$ ,  $m$  and  $n$  are determined by the results of experiment. In this work, we choose  $m = n = 1$ . Considering the thermal initiation, the Cochran model and initiation condition are written as below

$$\frac{d\lambda}{dt} = \begin{cases} \omega_1 P^m (1 - \lambda) + \omega_2 P^n \lambda (1 - \lambda) & \text{for } T \geq T_{th} , \\ 0 & \text{for } T < T_{th} , \end{cases} \quad (29)$$

where  $T_{th}$  is the temperature threshold for chemical reaction. In this work, we choose  $T_{th} = 1.1$ .

Via the operator-splitting scheme, eq.(28) can be decomposed into the following three subequations,

$$\begin{cases} \frac{\partial \lambda}{\partial t} - \omega_1 P^m (1 - \lambda) - \omega_2 P^n \lambda (1 - \lambda) = 0 \\ \frac{\partial \lambda}{\partial t} + u_r \frac{\partial \lambda}{\partial r} = 0 \\ \frac{\partial \lambda}{\partial t} + \frac{1}{r} u_\theta \frac{\partial \lambda}{\partial \theta} = 0. \end{cases} \quad (30)$$

Via introducing the symbol,  $a = \omega_1 P^m$ ,  $b = \omega_2 P^n$ ,  $\lambda = \lambda(t)$ ,  $\lambda_t^* = \lambda(t + dt)$ , we get the following analytic solution

$$\lambda_t^* = \frac{(a + b\lambda)e^{(a+b)dt} - a(1 - \lambda)}{(a + b\lambda)e^{(a+b)dt} + a(1 - \lambda)}, \quad (31)$$

from the first subequation. By introducing the symbol,  $\lambda_{i_r}^* = \lambda(i_r, t + dt)$ ,  $\lambda_{i_r} = \lambda(i_r, t)$ ,  $\lambda_{i_\theta}^* = \lambda(i_\theta, t + dt)$ ,  $\lambda_{i_\theta} = \lambda(i_\theta, t)$ , the last two subequations in Eq.(30) can be solved by the first order upwind scheme,

$$\frac{\lambda_{i_r}^* - \lambda_{i_r}}{\Delta t} = \begin{cases} -\frac{u_r(\lambda_{i_r} - \lambda_{i_r-1})}{\Delta r} & \text{for } u_r \geq 0, \\ -\frac{u_r(\lambda_{i_r+1} - \lambda_{i_r})}{\Delta r} & \text{for } u_r < 0, \end{cases} \quad (32)$$

$$\frac{\lambda_{i_\theta}^* - \lambda_{i_\theta}}{\Delta t} = \begin{cases} -\frac{u_\theta(\lambda_{i_\theta} - \lambda_{i_\theta-1})}{r\Delta\theta} & \text{for } u_\theta \geq 0, \\ -\frac{u_\theta(\lambda_{i_\theta+1} - \lambda_{i_\theta})}{r\Delta\theta} & \text{for } u_\theta < 0. \end{cases} \quad (33)$$

By composing the results in Eqs.(31), (32) and (33), we get

$$\lambda^{t+\Delta t} = \lambda_t^* + (\lambda_{i_r}^* - \lambda) + (\lambda_{i_\theta}^* - \lambda). \quad (34)$$

More accurate operator splitting schemes are shown in Appendix.

### 3.3. released chemical energy

In the detonation progress the released chemical energy of reaction, in the form of heat, is added to the internal energy, i.e.

$$E^{new} = E + (\lambda^{new} - \lambda)\rho q, \quad (35)$$

where  $\lambda$  is the parameter before local chemical reaction,  $\lambda^{new}$  is the one after local chemical reaction within one time step  $\Delta t$ ,  $(\lambda^{new} - \lambda)\rho q$  is the released chemical energy,  $E$  is internal energy before reaction,  $E^{new}$  is the renew internal energy after reaction, meanwhile pressure  $P$  and temperature  $T$  change with the updated  $E^{new}$ . Then we calculate the local equilibrium distribution function  $f_{ki}^{eq}$  from the updated physical quantities. To this step, the chemical reaction has coupled naturally with the flow behavior.

It should be pointed out that the renew internal energy  $E^{new}$  and the parameter  $\lambda^{new}$  are at the same time, the internal energy  $E$  and the parameter  $\lambda$  are at the same time. Overall, internal energy changes twice in the simulation of detonation, the former satisfies the Hugoniot relations for shock, the latter satisfies the relation in eq.(35). Correspondingly, the parameter for chemical reaction progress changes twice, the former comes from the convection process as shown in the last two subequations in eq.(30), the latter comes from the chemical reaction process as shown in the first subequation in eq.(30). Consequently, the variation of parameter for chemical reaction progress in eq.(35) is  $(\lambda^{new} - \lambda) = (1 - \lambda)(\omega_1 p^m + \omega_2 \lambda p^n) \times dt$ .

### 3.4. Simulation of detonation

*3.4.1. validation and verification* In order to demonstrate the validity of the new model, we numerically simulate the propagation of steady detonation. The initial macroscopic quantities are set as below:

$$\begin{cases} (\rho, T, u_r, u_\theta, \lambda)_{inner} = (1.35826, 2.59709, 0.81650, 0, 1) \\ (\rho, T, u_r, u_\theta, \lambda)_{outer} = (1, 1, 0, 0, 1) \end{cases} \quad (36)$$

which satisfy the Hugoniot relations in eq.(25). Here the suffixes *inner* and *outer* index two parts,  $10000 \leq r \leq 10000.1$  and  $10000.1 < r \leq 10002$ , in an annular area, respectively. It should be pointed out that the inner radius is given as large enough here. With this condition, the simulation results below could be compared to the analytic solutions in eq.(27). Other parameters are  $\tau = 10^{-7}$ ,  $N_r \times N_\theta = 2000 \times 3$ ,  $\omega_1 = 1$ ,  $\omega_2 = 50$ . The initial conditions in eq.(36) could trigger the detonation. After initial stage of initiation and development, detonation becomes a steady one propagating forwards step by step. Now we use physical quantities of steady detonation as the initial conditions to restart the simulation, see Fig.3, where we obtain the velocity of detonation wave  $D = 3.08$ . Compared with the analytic solution  $D = 3.09557$ , the relative difference is 0.5%. Other physical quantities after detonation wave are  $(\rho, T, u_r, u_\theta, \lambda) = (1.36128, 2.58909, 0.818334, 0, 1)$ . Compared with the values of the left hand side of the first line in eq.(36), the relative differences are 0.2%, 0.3%, 0.2%, 0% and 0%, respectively. Simulation results fully indicate that the LB model works for simulating the shock initiation of detonation.

Figure 4 gives the physical quantities versus radius, corresponding to Fig. 3 at time  $t = 0.25$ , with radial range  $10000.85 \leq r \leq 10000.95$ . Three vertical lines are shown, from left to right, to guide the eyes for the rarefaction area, the maximum value of pressure, the pre-shocked area, respectively. There is strong compression around the rightmost line, which increases physical quantities suddenly. On the contrary, the rarefaction effect around the leftmost line reduce physical quantities relatively slowly. In addition, it's easy to find that the maximum values of density, temperature, pressure, velocity do not exactly coincide. The radial positions of their maximum values are  $R_\rho = 10000.9195$ ,  $R_T = 10000.9045$ ,  $R_P = 10000.9175$ ,  $R_u = 10000.9195$ .

*3.4.2. implosion* Implosion and explosion are two forms of detonation phenomena in a round area. For the case of implosion, the initial physical quantities are set as below:

$$\begin{cases} (\rho, T, u_r, u_\theta, \lambda)_{inner} = (1, 1, 0, 0, 0) \\ (\rho, T, u_r, u_\theta, \lambda)_{outer} = (1.5, 1.55556, -0.666667, 0, 1) \end{cases} \quad (37)$$

which satisfy the Hugoniot relations of shock wave. Here the suffixe *inner* indexes area  $0 \leq r \leq 0.098$ , where is pre-reacted reactant. The suffixe *outer* indexes area  $0.098 < r \leq 0.1$ , where is reacted reactant. Other parameters are  $\tau = 10^{-5}$ ,  $N_r \times N_\theta = 100 \times 3$ ,  $\omega_1 = 1$ ,  $\omega_2 = 100$ .

Figure 5 shows physical quantities along radius in implosion process at times,  $t = 0.000, 0.039, 0.042$  and  $0.060$ , respectively: (a) density; (b) temperature; (c)

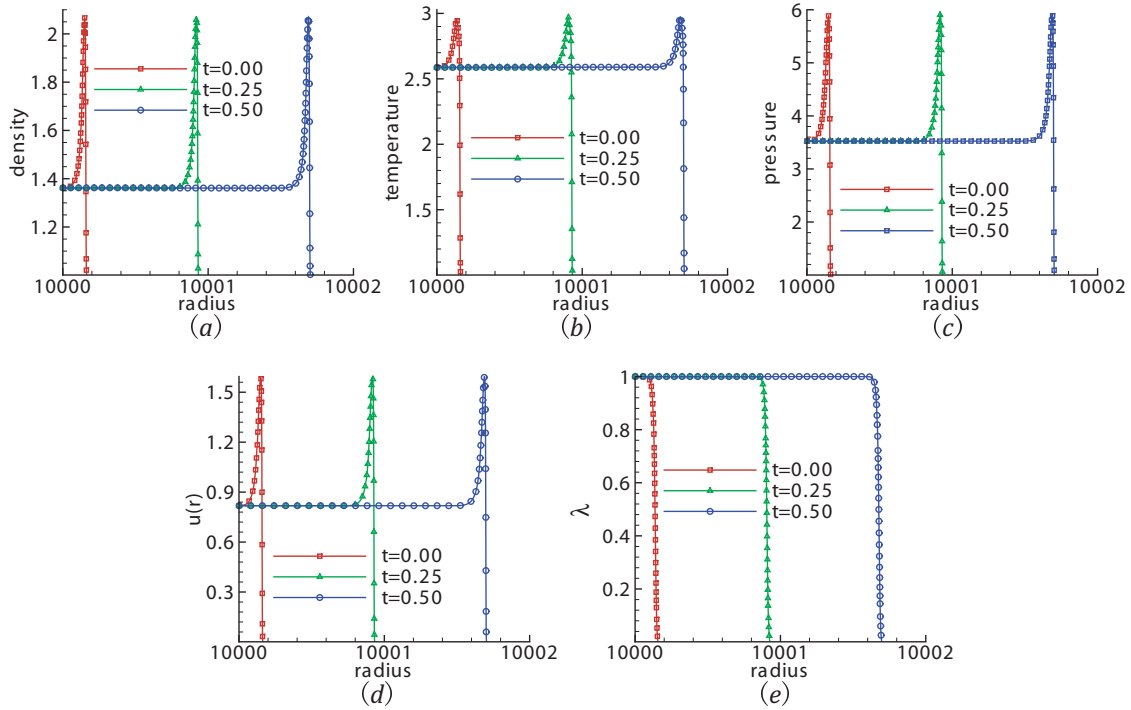


**Figure 3.** Physical quantities in steady detonation wave within an annular area with radii  $R_1 = 10000$  and  $R_2 = 10002$  at times,  $t = 0.00, 0.25, 0.50$ . (a) density; (b) temperature; (c) pressure; (d) radial velocity  $u_r$ ; (e) the parameter for chemical reaction process  $\lambda$ .

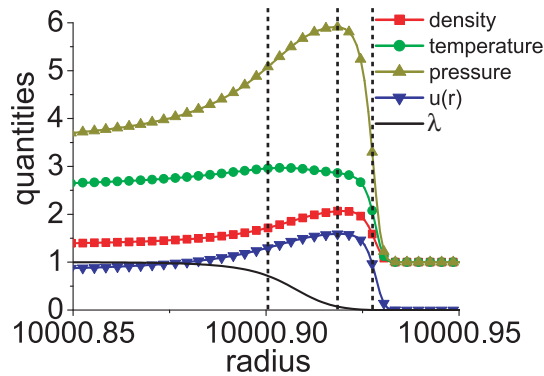


**Figure 4.** Physical quantities in steady detonation wave within an annular area with radii  $R_1 = 10000$  and  $R_2 = 10002$  at time  $t = 0.25$ . From left to right, three vertical lines are shown to guide the eyes for the rarefaction area, the maximum value of pressure, the pre-shocked area, respectively.

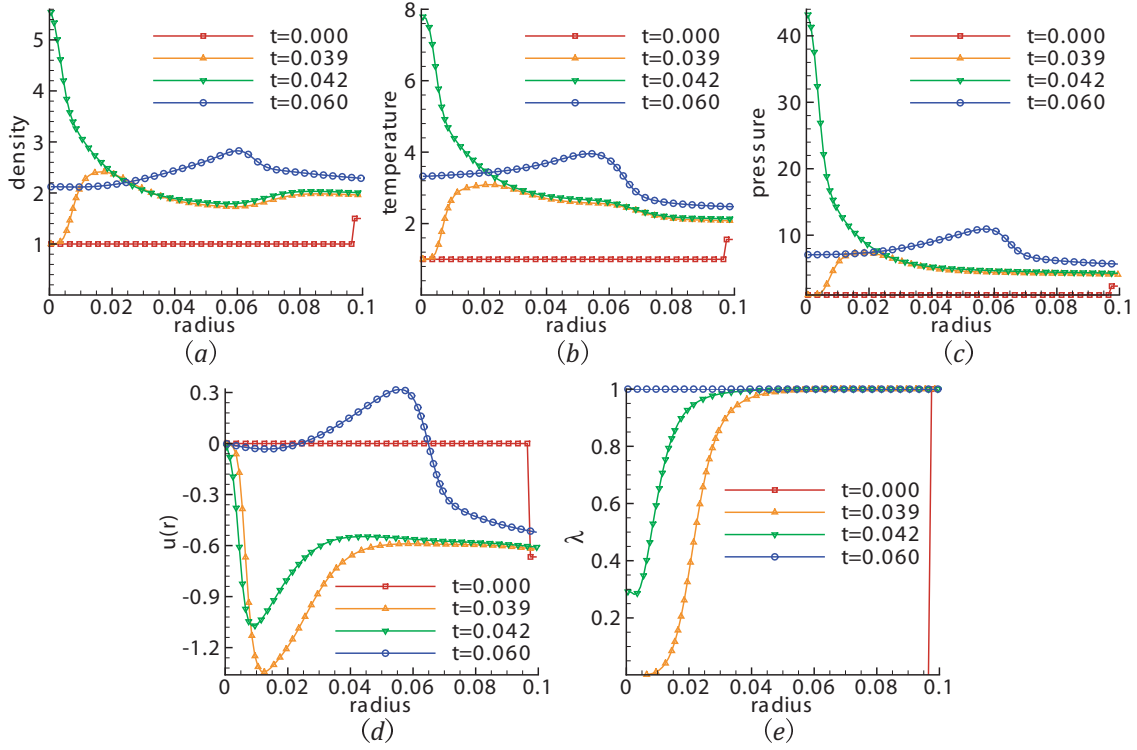


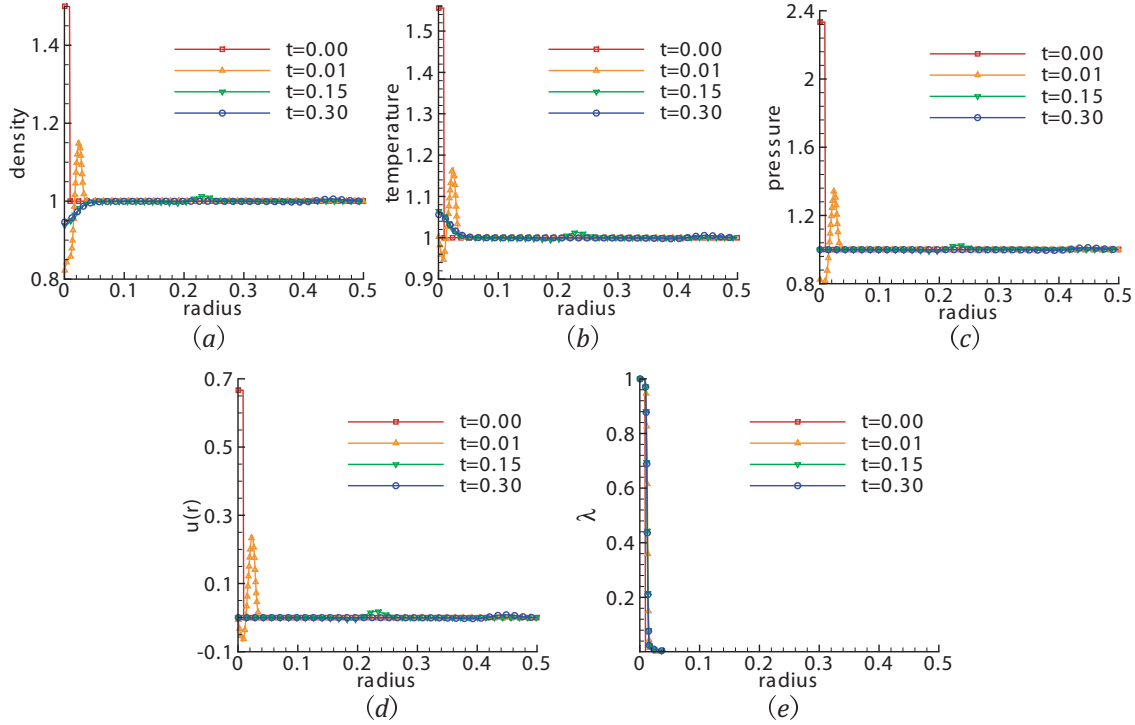
**Figure 5.** Physical quantities versus radius in implosion process at times,  $t = 0.000$ ,  $0.039$ ,  $0.042$  and  $0.060$ , respectively: (a) density; (b) temperature; (c) pressure; (d) radial velocity  $u_r$ ; (e) the parameter for chemical reaction process  $\lambda$ .

pressure; (d) radial velocity  $u_r$ ; (e) the parameter for chemical reaction process  $\lambda$ . There are two stages in the implosion process. In the former stage, the detonation travels inwards. A large number of particles move inwards after compression of detonation, and the density, temperature and pressure behind detonation wave increase continuously due to geometric effect of the round area which is an enclosed space. When the detonation wave reaches the center, the density, temperature and pressure increase monotonically along radius. Meanwhile, the velocity inwards reduces to zero gradually and then point outwards. In the latter stage, the detonation wave travels outwards. As the chemical reaction completes, the detonation wave eventually turns into a shock wave. The velocity before the shock front points inwards and the one after the shock front points outwards. So the density, temperature and pressure before shock front are still increasing continuously, and those behind the front will reduce.

*3.4.3. explosion* Now let's simulate the explosion. The initial macroscopic quantities are set as below:

$$\begin{cases} (\rho, T, u_r, u_\theta, \lambda)_{inner} = (1.5, 1.55556, 0.666667, 0, 1) \\ (\rho, T, u_r, u_\theta, \lambda)_{outer} = (1, 1, 0, 0, 0) \end{cases} \quad (38)$$

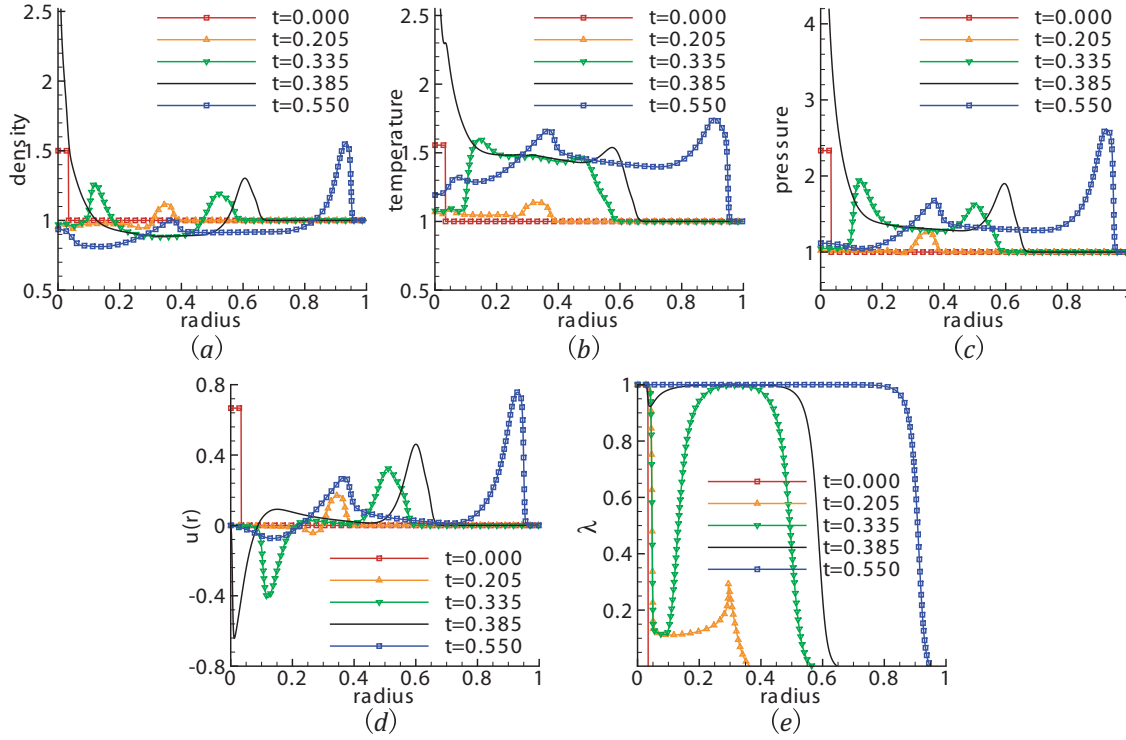
where the suffix *inner* indexes area  $0 \leq r \leq R_1$ , the suffix *outer* indexes area  $R_1 < r \leq R$ . The *inner* area is full of reacted reactant and the *outer* area is filled with



**Figure 6.** For the case  $R_1 = 0.010$ , physical parameters versus radius in explosion process at times,  $t = 0.00, 0.01, 0.15$  and  $0.30$ , respectively: (a) density; (b) temperature; (c) pressure; (d) radial velocity  $u_r$ ; (e) the parameter for chemical reaction process  $\lambda$ .

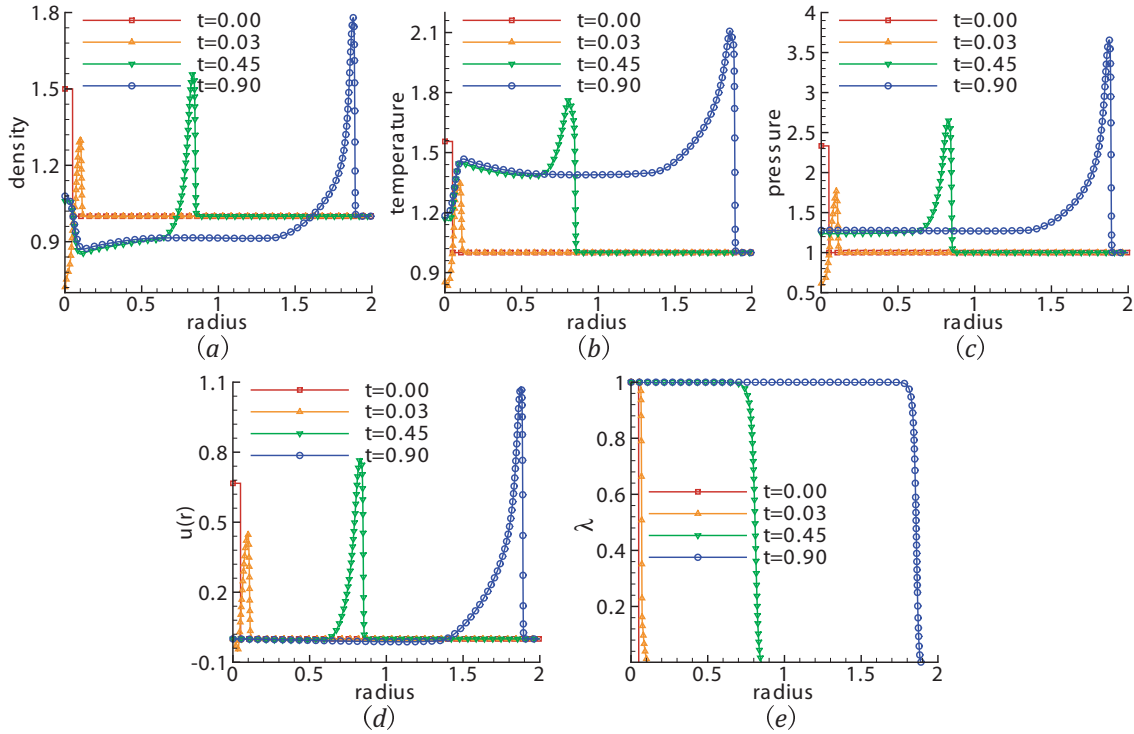
pre-reacted reactant. We choose  $\tau = 10^{-5}$ ,  $\omega_1 = 1$ ,  $\omega_2 = 50$  here. Fig.6 corresponds to parameters  $R_1 = 0.010$ ,  $R = 0.5$ ,  $N_r \times N_\theta = 500 \times 3$ ; Fig.7 corresponds to parameters  $R_1 = 0.034$ ,  $R = 1.0$ ,  $N_r \times N_\theta = 1000 \times 3$ ; Fig.8 corresponds to parameters  $R_1 = 0.050$ ,  $R = 2.0$ ,  $N_r \times N_\theta = 2000 \times 3$ .

Figure 6 shows physical parameters versus radius at times,  $t = 0.00, 0.01, 0.15$  and  $0.30$ , respectively: (a) density  $\rho$ ; (b) temperature  $T$ ; (c) pressure  $P$ ; (d) radial velocity  $u_r$ ; (e) the parameter for chemical reaction process  $\lambda$ . The area of initial reacted reaction is small, where the initial energy is not enough to trigger the detonation. Then the energy propagates outward in the form of disturbance whose amplitude reduces gradually, then dissipates and disappears finally. The disturbance spreads outward in the form of wave. It compresses media in front of wave front, where the density, temperature, pressure and velocity increase and wave crest appears. On the contrary, it has a rarefaction effect behind wave front, where those physical quantities reduce and wave trough appears. It's easy to get from Fig.(e) that  $\lambda$  has only a little change at the beginning, then doesn't change any longer. The reason is that the initial temperature of reacted reaction is higher than the temperature threshold  $T_{th}$  and there is a little chemical reaction at the start. The rate of chemical energy released is smaller than the rate of heat dissipated. So the energy of disturbance wave is less and less, and finally leads to extinguishment.



**Figure 7.** For the case  $R_1 = 0.034$ , physical parameters versus radius in explosion process at times,  $t = 0.000, 0.205, 0.335, 0.385$  and  $0.550$ , respectively: (a) density; (b) temperature; (c) pressure; (d) radial velocity  $u_r$ ; (e) the parameter for chemical reaction process  $\lambda$ .

Figure 7 shows physical parameters versus radius at times,  $t = 0.000, 0.205, 0.335, 0.385$  and  $0.550$ , respectively. It can be divided into four stages in the evolution shown in Fig.7. The first stage from  $t = 0.000$  to  $0.205$  is the process of propagation and development of “perturbation wave”. The chemical reaction is going on and is not complete. Only part of the reaction reacts. The released chemical energy is added to the “perturbation zone”, meanwhile thermal energy within “perturbation zone” spreads to adjacent area. There is competitive relationship between the two mechanisms. The energy within “perturbation zone” and the width of “perturbation zone” along radius increase, and the maximum values of density, temperature, pressure and velocity fall. The rate of released chemical energy is larger than that of diffusion. The second stage from  $t = 0.205$  to  $0.335$  is the process of transformation from “perturbation wave” to “detonation wave”. The rate of chemical energy released is accelerated sharply, which increases density, temperature, pressure and velocity suddenly. Meanwhile the increase of pressure (or/and temperature) will accelerate the rate of chemical reaction further. The rate of chemical energy released is larger than the rate of heat dissipated. The third stage from  $t = 0.335$  to  $0.385$  is the development process of detonation waves, i.e. implosion wave and explosion wave. The fourth stage from  $t = 0.385$  to  $0.550$  is the propagation process of detonation wave. The implosion wave has passed the center of round, then travels outwards and changes into shock wave when chemical



**Figure 8.** For the case  $R_1 = 0.034$ , physical parameters versus radius in explosion process at times,  $t = 0.00, 0.03, 0.45$  and  $0.90$ , respectively: (a) density; (b) temperature; (c) pressure; (d) radial velocity  $u_r$ ; (e) the parameter for chemical reaction process  $\lambda$ .

reaction completes. The shock wave changes into “perturbation wave” step by step, then dissipates and disappears finally. While the explosion wave propagates outwards and its peak rises further.

Figure 8 shows physical parameters versus radius at times,  $t = 0.00, 0.03, 0.45$  and  $0.90$ , respectively. Figure (a) shows the density behind wave is lower than that in front. Figure (b) shows the temperature behind wave is higher than that in front. Figure (c) shows that the pressure behind wave front is a little higher than that in front, and the pressure gradient behind wave is quite small. Figure (d) shows that the velocity behind wave is approximately equal to zero. Figure (e) shows that chemical reaction steadily goes forwards. From figures (a)-(e) we can find that the energy of within initial reacted reaction is large enough to trigger detonation directly. System is in equilibrium state before wave and gradually becomes close to equilibrium state after wave. The detonation wave zone becomes wider and wider along radius, where values of physical quantities increase continuously, and the values in von-Neumann-peak rise gradually. Physical quantities in front of the peak increase sharply with large gradient due to shock effect, and those behind wave front fall slowly with smaller gradient due to rarefaction effect. In addition, physical quantities around von-Neumann-peak rise less slowly due to the geometric effect of round which is a closed region after detonation wave, and detonation wave will not propagate stably.

#### 4. Non-equilibrium characteristics in steady detonation

Boltzmann equation is a basic equation describing non-equilibrium system. LB model naturally inherits the property and function of Boltzmann equation describing non-equilibrium process. In this section we study the non-equilibrium characteristics.

Among the seven moment relations, Eqs.(8)-(14), the local equilibrium distribution function  $f_{ki}^{eq}$  can be replaced by the distribution function  $f_{ki}$  for the first three. If we replace  $f_{ki}^{eq}$  by  $f_{ki}$  in Eqs.(11)-(14), the left and right hand sides of Eqs.(11)-(14) will no longer be equal. This mismatch measures departure of the non-equilibrium system from local thermodynamic equilibrium. Two kinds of space-time dependent fields, moments  $\mathbf{M}_m$  and central moments  $\mathbf{M}_m^*$  are defined as below:

$$\begin{cases} \mathbf{M}_2(f_{ki}) = \sum_{ki} f_{ki} \mathbf{v}_{ki} \mathbf{v}_{ki} \\ \mathbf{M}_3(f_{ki}) = \sum_{ki} f_{ki} \mathbf{v}_{ki} \mathbf{v}_{ki} \mathbf{v}_{ki} \\ \mathbf{M}_{3,1}(f_{ki}) = \sum_{ki} \frac{1}{2} f_{ki} \mathbf{v}_{ki} \cdot \mathbf{v}_{ki} \mathbf{v}_{ki} \\ \mathbf{M}_{4,2}(f_{ki}) = \sum_{ki} \frac{1}{2} f_{ki} \mathbf{v}_{ki} \cdot \mathbf{v}_{ki} \mathbf{v}_{ki} \mathbf{v}_{ki} \end{cases} \quad (39)$$

$$\begin{cases} \mathbf{M}_2^*(f_{ki}) = \sum_{ki} f_{ki} (\mathbf{v}_{ki} - \mathbf{u})(\mathbf{v}_{ki} - \mathbf{u}) \\ \mathbf{M}_3^*(f_{ki}) = \sum_{ki} f_{ki} (\mathbf{v}_{ki} - \mathbf{u})(\mathbf{v}_{ki} - \mathbf{u})(\mathbf{v}_{ki} - \mathbf{u}) \\ \mathbf{M}_{3,1}^*(f_{ki}) = \sum_{ki} \frac{1}{2} f_{ki} (\mathbf{v}_{ki} - \mathbf{u}) \cdot (\mathbf{v}_{ki} - \mathbf{u})(\mathbf{v}_{ki} - \mathbf{u}) \\ \mathbf{M}_{4,2}^*(f_{ki}) = \sum_{ki} \frac{1}{2} f_{ki} (\mathbf{v}_{ki} - \mathbf{u}) \cdot (\mathbf{v}_{ki} - \mathbf{u})(\mathbf{v}_{ki} - \mathbf{u})(\mathbf{v}_{ki} - \mathbf{u}). \end{cases} \quad (40)$$

The moment  $\mathbf{M}_{3,1}(= M_{3,1,\alpha} \mathbf{e}_\alpha)$  is a vector with two components,  $M_{3,1,r}$  and  $M_{3,1,\theta}$ . The moment  $\mathbf{M}_2(= M_{2,\alpha\beta} \mathbf{e}_\alpha \mathbf{e}_\beta)$  is a 2-order tensor with four components, among which only three,  $M_{2,rr}$ ,  $M_{2,r\theta}$  and  $M_{2,\theta\theta}$ , are independent. The case for the moment  $\mathbf{M}_{4,2}(= M_{4,2,\alpha\beta} \mathbf{e}_\alpha \mathbf{e}_\beta)$  is similar. The moment  $\mathbf{M}_3(= M_{3,\alpha\beta\gamma} \mathbf{e}_\alpha \mathbf{e}_\beta \mathbf{e}_\gamma)$  is a 3-order tensor with eight components, and only four,  $M_{3,rrr}$ ,  $M_{3,rr\theta}$ ,  $M_{3,r\theta\theta}$  and  $M_{3,\theta\theta\theta}$ , are independent. The central moments  $\mathbf{M}_m^*$  is mathematically similar to  $\mathbf{M}_m$ .

For one-dimensional distribution function  $f(v)$ , in probability theory,  $M_3^* = \int dv f(v)(v - u)^3$  is “skewness”,  $M_4^* = \int dv f(v)(v - u)^4$  is “kurtosis” describing the “flatness” of the distribution  $f(v)$ . For a Gaussian distribution function,  $f(v) = 1/\sqrt{2\pi} \exp[-(v - u)^2/2]$ ,  $M_4^* = 3$ . For the case with  $M_4^* > 3$  and  $M_2^* = 1$ , the distribution is sharper than the Gaussian at the central position.

Physically, the moments  $\mathbf{M}_2$  and  $\mathbf{M}_3$  are 2-times and 3-times associations of “particle fluctuation” in different degrees of freedom, respectively. The moment  $\mathbf{M}_{3,1}$  is a contraction of 3-times association of “particle fluctuation”, and  $\mathbf{M}_{4,2}$  is a contraction of 4-times association. For the matrixes of  $\mathbf{M}_2$  and  $\mathbf{M}_2^*$ , their traces are conservations associating with temperature and their off-diagonal components associate with the shear effects. If the system is equilibrium, the off-diagonal components are zero, else they may not be zero. The moments  $\mathbf{M}_3$  and  $\mathbf{M}_{3,1}$  describe mixtures of two physical quantities: energy flux caused by macroscopic fluid flow and “energy flow of microscopic fluctuation”. The central moments  $\mathbf{M}_3^*$  and  $\mathbf{M}_{3,1}^*$  describe “energy flow of microscopic fluctuation” in non-equilibrium progress, such as thermal diffusion, viscosity etc. For equilibrium system,  $\mathbf{M}_3^* = 0$  and  $\mathbf{M}_{3,1}^* = 0$ . For non-equilibrium system where is “energy

flow of microscopic fluctuation”,  $\mathbf{M}_3^* \neq 0$  and  $\mathbf{M}_{3,1}^* \neq 0$ . Because the distribution function satisfies  $f(\mathbf{v}) = f(-\mathbf{v})$  in equilibrium state, while  $f(\mathbf{v}) \neq f(-\mathbf{v})$  in non-equilibrium state. This breaking of symmetry in non-equilibrium progress results in eventually transport heat without necessarily carrying a net flow.

The manifestations of non-equilibrium are defined as below:

$$\Delta_m = \mathbf{M}_m(f_{ki}) - \mathbf{M}_m(f_{ki}^{eq}) = \mathbf{M}_m(f_{ki} - f_{ki}^{eq}), \quad (41)$$

$$\Delta_m^* = \mathbf{M}_m^*(f_{ki}) - \mathbf{M}_m^*(f_{ki}^{eq}) = \mathbf{M}_m^*(f_{ki} - f_{ki}^{eq}). \quad (42)$$

Here the moment  $\mathbf{M}_m$  contains information of macroscopic flow velocity  $\mathbf{u}$ , while the central moment  $\mathbf{M}_m^*$  is only the manifestation of thermo-fluctuations of molecules relative to the macroscopic flow velocity  $\mathbf{u}$ .  $\Delta_m$  and  $\Delta_m^*$  are similar to  $\mathbf{M}_m$  and  $\mathbf{M}_m^*$ .

#### 4.1. Simulation results and analysis

Non-equilibrium in the evolution of detonation is extremely complex. For simplicity, we investigate central moments and their corresponding non-equilibrium manifestations in the progress of steady detonation with respect to Fig.4. Figure 9 shows the simulation results of  $\mathbf{M}_m^*$  and  $\Delta_m^*$ . Figures (a)-(d) are for  $\mathbf{M}_2^*(f)$ ,  $\mathbf{M}_3^*(f)$ ,  $\mathbf{M}_{3,1}^*(f)$ ,  $\mathbf{M}_{4,2}^*(f)$ , respectively. Figures (e)-(h) are for  $\mathbf{M}_2^*(f^{eq})$ ,  $\mathbf{M}_3^*(f^{eq})$ ,  $\mathbf{M}_{3,1}^*(f^{eq})$ ,  $\mathbf{M}_{4,2}^*(f^{eq})$ , respectively. Figures (i)-(l) are for deviations  $\Delta_2^*$ ,  $\Delta_3^*$ ,  $\Delta_{3,1}^*$ ,  $\Delta_{4,2}^*$ , respectively. Figures (m)-(p) are enlargements corresponding to the portions labeled by rectangles in (i)-(l), respectively. Only independent components of  $\mathbf{M}_m^*$  and  $\Delta_m^*$  are shown. The specific correspondences are referred to the legends. The three vertical lines in each plot coincide with the ones in Fig.4.

From Fig.9, we can find the following features:

First, around the von-Neumann peak, the system starts to deviate from thermodynamic equilibrium once physical quantities ( $\rho, T, P, u_r$ ) begin to increase and finally reaches its thermodynamic equilibrium as those quantities attains their steady values required by the Hugoniot relations in Eq.(25).

Second, the departure of system from its equilibrium around the leftmost line and the one around the rightmost line are in opposite directions. Around the leftmost line, the system experiences a sudden deviation from thermodynamic equilibrium, due to the strong compression from the reaction product behind the von-Neumann peak. Around the rightmost line, the system deviate from thermodynamic equilibrium in the opposite direction, due to the rarefaction effect.

Third, during the non-equilibrium progress,  $\Delta_{2,rr}^*$  and  $\Delta_{2,\theta\theta}^*$  show peaks, in opposite directions with the same amplitude, i.e.  $\Delta_{2,rr}^* + \Delta_{2,\theta\theta}^* = 0$ , which results from energy conservation. Around the rightmost line,  $\Delta_{2,rr}^* > 0$  and  $\Delta_{2,\theta\theta}^* < 0$ . Physically, the mean kinetic energy  $\int d\mathbf{v} f (v_r - u_r)^2 / 2$ , which can be named the internal kinetic energy in the radial degree of freedom here, increases first. Then, part of internal kinetic energy variance is transferred to other degrees of freedoms via collisions of molecules. Then, the internal kinetic energy in this degree of freedom further varies according to compression from the detonation behind, and so on. Around the leftmost line,  $\Delta_{2,rr}^* < 0$

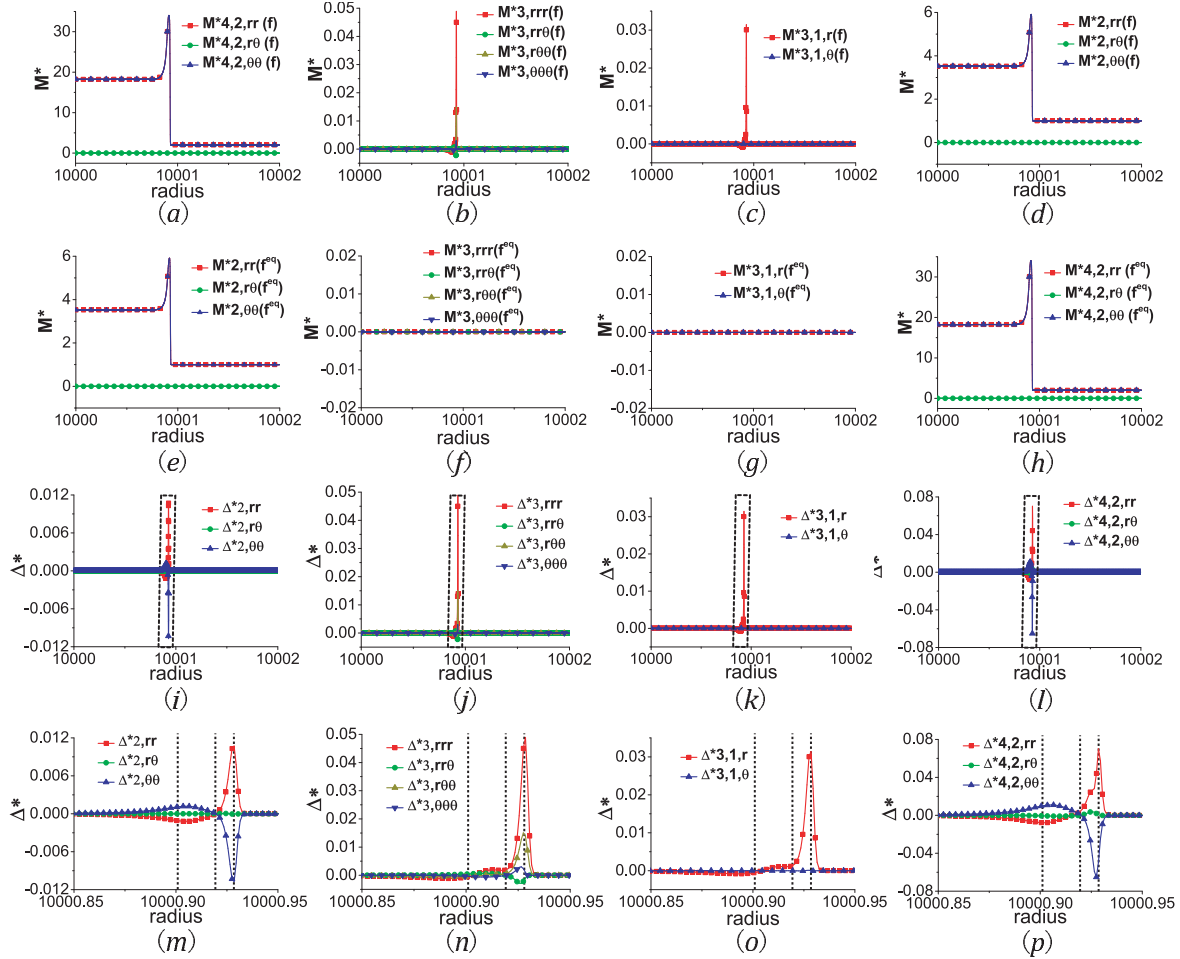


**Figure 9.** Central moments and their corresponding non-equilibrium manifestations in stable propagation of detonation wave within an annular area with radii  $R_1 = 10000$  and  $R_2 = 10002$  at time  $t = 0.25$ . Figures (a)-(d) are for  $M_2^*(f)$ ,  $M_3^*(f)$ ,  $M_{3,1}^*(f)$ ,  $M_{4,2}^*(f)$ , respectively. Figures (e)-(h) are for  $M_2^*(f^{eq})$ ,  $M_3^*(f^{eq})$ ,  $M_{3,1}^*(f^{eq})$ ,  $M_{4,2}^*(f^{eq})$ , respectively. Figures (i)-(l) are for deviations  $\Delta_2^*$ ,  $\Delta_3^*$ ,  $\Delta_{3,1}^*$ ,  $\Delta_{4,2}^*$ , respectively. Figures (m)-(p) correspond to the portions labeled by rectangles in (i)-(l), respectively. Only independent components of  $M_m^*$  and  $\Delta_m^*$  are shown. The specific correspondences are referred to the legends. The vertical lines Figs.(m)-(p) coincide with the ones in Fig.4

and  $\Delta_{2,\theta\theta}^* > 0$ , which can be interpreted in a similar way. Only when the system attain its thermodynamic equilibrium, the internal kinetic energy in different degrees of the freedom equal to each other.

Fourth, the values of  $\Delta_2^*$ ,  $\Delta_3^*$ ,  $\Delta_{3,1}^*$ ,  $\Delta_{4,2}^*$  are zero in equilibrium state, and their values around the rightmost line are much higher than those around the leftmost line. This is because the shocking process is very quick, the pre-shock area is very thin. The changing rates of macroscopic quantities are very high. The system has very little time to relax to its thermodynamic equilibrium and has also very little time for the thermo diffusion. But the interface of rarefaction area is much wider. The system around the leftmost line is much closer to its thermodynamic equilibrium.

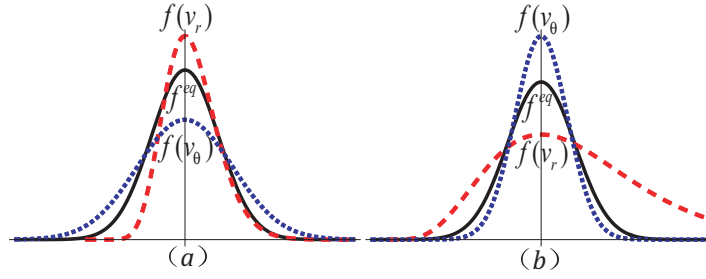


**Figure 10.** The sketch of the Maxwellian and actual distribution functions versus velocity  $v_r$  and  $v_\theta$ , respectively. (a) the distribution functions at the leftmost line, (b) the distribution functions at the rightmost line. The long-dashed line is for distribution function  $f(v_r)$ , the shot-dashed one is for distribution function  $f(v_\theta)$ , and the solid line is for  $f^{eq}$ .

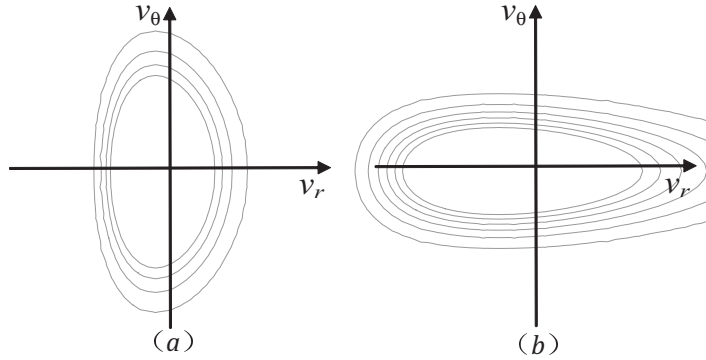


**Figure 11.** The sketch of contours of the actual distribution functions in velocity space  $(v_r, v_\theta)$ . Figure (a) and (b) show the recovered distribution function contours at the leftmost and rightmost line, respectively.

Fifth, the value of  $\Delta_{2,r\theta}^*$  equals to zero. It is because the physical field under consideration is the same along the circumferential direction. Consequently, there is no shear viscous effects except for error in numerical calculation.

Sixth, in theory and simulation,  $\mathbf{M}_3^*(f^{eq}) = 0$  and  $\mathbf{M}_{3,1}^*(f^{eq}) = 0$ , so  $\mathbf{M}_3^*(f) = \Delta_3^*$  and  $\mathbf{M}_{3,1}^*(f) = \Delta_{3,1}^*$ . Then we can find that the simulation results of  $\mathbf{M}_3^*(f)$  and  $\mathbf{M}_{3,1}^*(f)$  in Fig.9(b) and (c) coincide with the values of  $\Delta_3^*$  and  $\Delta_{3,1}^*$  in Fig.9(f) and (g).

Finally, it should be pointed out that, the non-equilibrium effects can be triggered by the gradient of anyone among density, momentum, pressure and temperature. The temporal or spacial changes of macroscopic physical quantities offer driving force to the emergence and development of non-equilibrium effects. And the non-equilibrium will also have an important influence on those physical quantities.

#### 4.2. Recovering of the distribution function

From the simulation results of deviations  $\Delta_m^*$  in Fig.9, we can draw qualitative information on the discrete distribution function and then recover qualitatively the actual distribution function. The main steps are given below.

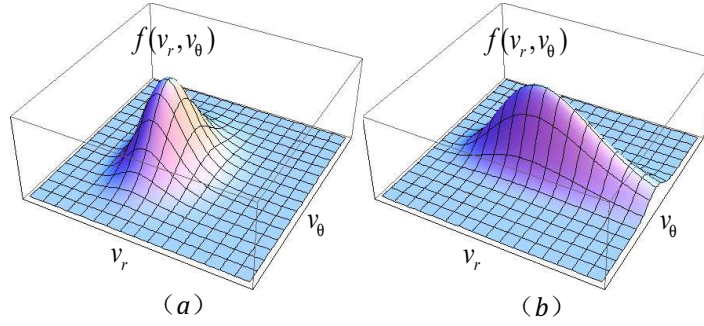


**Figure 12.** The sketches of the actual distribution functions in velocity space  $(v_r, v_\theta)$ . Figures (a) and (b) show the recovered distribution functions at the leftmost and rightmost lines, respectively.

Step one: we consider the actual functions  $f(v_r)$  and  $f(v_\theta)$  at the rarefaction area around the leftmost line where  $\Delta_{2,rr}^*$  shows a negative peak and  $\Delta_{2,\theta\theta}^*$  shows a positive peak with the same amplitude. Up to this step, we can conclude that the distribution function  $f(v_r)$  is “thinner” and  $f(v_\theta)$  is “fatter” than the Maxwellian  $f^{eq}$ , which is a normal distribution function describing the equilibrium. The peak of  $f(v_r)$  is higher and the peak of  $f(v_\theta)$  is lower than that of the Maxwellian.  $\Delta_{4,2}^*$  in Fig.9 (l) shows complementary information to  $\Delta_2^*$  in Fig.9(i).

From the simulation results of  $\Delta_3^*$  in Fig.9(j) and  $\Delta_{3,1}^*$  in Fig.9(k), we can obtain that  $f(v_\theta)$  is symmetric, while the  $f(v_r)$  is asymmetric. The portion of  $f(v_r)$  for  $v_r > 0$  is “fatter” than that for  $v_r < 0$ , which is often named “positive skewness”. Figure 10 (a) shows the sketch of the actual distribution functions,  $f(v_r)$ ,  $f(v_\theta)$  and the Maxwellian  $f^{eq}$  at the leftmost line. According to the symmetry of  $f^{eq}$ , we know that  $f^{eq}(v_r)$  and  $f^{eq}(v_\theta)$  coincide in Fig.10(a). Similarly, Fig.10(b) shows the sketch of the actual distribution functions,  $f(v_r)$ ,  $f(v_\theta)$  and the Maxwellian  $f^{eq}$  at the rightmost line, where  $f(v_r)$  is “fatter” and  $f(v_\theta)$  is “thinner” than the Maxwellian  $f^{eq}$ . The peak of  $f(v_r)$  is lower and the peak of  $f(v_\theta)$  is higher than that of  $f^{eq}$ .  $f(v_\theta)$  is symmetric, while  $f(v_r)$  is asymmetric. The portion of  $f(v_r)$  for  $v_r > 0$  is “fatter” and the portion of  $f(v_r)$  for  $v_r < 0$  is “thinner”.

Step two: we analyse the contours of the actual distribution function in two-dimensional velocity space  $(v_r, v_\theta)$ . As shown in Fig.9(i),  $\Delta_{2,r\theta}^* = 0$ , it implies that the contours of the actual distribution function within the whole area ought to be symmetric in  $v_r$  or/and  $v_\theta$ . With the analysis in step one, the symmetry of  $f(v_\theta)$  and the asymmetry of  $f(v_r)$ , we can confirm that the  $v_r$  coordinate axis is the symmetric axis for the contour. Figures 9(l) shows consistent information. Figure 11 shows the sketches of contours of the actual distribution function at the leftmost line in (a) and at the rightmost line in (b), respectively.

Step three: by combining the results of the above two steps, we obtain the qualitative curves for the actual distribution functions at the two lines. Figure 12 shows qualitatively the sketches of the actual distribution functions in three dimensions. Figure (a) and (b) show the ones at the leftmost and rightmost lines, respectively.

## 5. Conclusions and discussions

A Polar Coordinate Lattice Boltzmann(PCLB) model for detonation phenomena is presented in this work. In this model the fluid behaviour is describe by a finite-difference lattice Boltzmann(FDLB) model in polar coordinates, and the chemical reaction is described by Cochran's rate function. For both the PDLB model and the Cochran's rate function, a key technique is that an operator-splitting scheme is used to treat with the temporal and spatial evolutions. Their temporal evolutions are calculated analytically and the convection terms are solved via the first-order upwind scheme.

For boundary conditions, ghost nodes are used. We use periodic conditions to treat with the two boundaries in the circumferential direction. Around the center point of round, the distribution functions on ghost nodes are given by rotation of those functions within physical area. For the outer boundary of a round and the radial boundaries of a circular area, we can use inflow and outflow conditions.

For the verification and validation, we compare the simulation results by the PCLB model with analytical solution of physical quantities in the steady detonation procedure. It's found that the simulation results have a satisfying agreement with analytical solutions. Then we investigate two kinds of detonation processes: implosion and explosion. By changing area of initial reacted reactant, we simulate the explosion in three cases. The area corresponds to the excitation energy triggering detonation. If the excitation energy is sufficient, the detonation can be triggered directly.

To show the merit of LB model over the traditional methods based on Navier-Stokes descriptions, we studied some non-equilibrium characteristics in the steady detonation. Numerical results show that, the amplitude of deviations from equilibrium in front of von-Neumann peak is much higher than those behind the peak. At the von-Neumann peak, the system is nearly in its thermodynamic equilibrium. By comparing each component of the high-order moments and its value in equilibrium, we draw qualitative information on the actual distribution functions at the compression area in front of von-Neumann peak and at the rarefaction area behind the peak, respectively. Such results are helpful for improving the traditional hydrodynamic models from a macroscopic level.

## Acknowledgements

The authors thank Profs. Guoxi Ni and Cheng Wang for many helpful discussions. AX and GZ acknowledge support of the Science Foundations of CAEP [under Grant Nos. 2012B0101014 and 2011A0201002] and the Foundation of State Key Laboratory of Explosion Science and Technology[under Grant No. KFJJ14-1M]. AX, GZ, YL and CL acknowledge support of National Natural Science Foundation of China [under Grant Nos. 11075021, 11074300, and 91130020]. YL and CL acknowledge support of National Basic Research Program of China (Grant No. 2013CBA01504).

## Appendix A. Appendices

In Eq.(18), the first subequation is an Ordinary Differential Equation (ODE) with exact solution, and the last two are Partial Differential Equations (PDEs), which can be calculated with different schemes.[32] We write Eq.(18) as

$$\begin{cases} \frac{\partial f_{ki}}{\partial t} = -\frac{1}{\tau} [f_{ki} - f_{ki}^{eq}] & \longrightarrow S_{feq} \\ \frac{\partial f_{ki}}{\partial t} + v_{kir} \frac{\partial f_{ki}}{\partial r} = 0 & \longrightarrow S_{fr} \\ \frac{\partial f_{ki}}{\partial t} + \frac{1}{r} v_{ki\theta} \frac{\partial f_{ki}}{\partial \theta} = 0 & \longrightarrow S_{f\theta} \end{cases} \quad (\text{A.1})$$

by introducing solution operators  $S_{feq}$ ,  $S_{fr}$  and  $S_{f\theta}$ . Then the three subequations in Eq.(A.1) can be solved in the following order with different Initial Conditions (ICs),

$$\left. \begin{array}{l} ODE : \frac{\partial f_{ki}}{\partial t} = -\frac{1}{\tau} [f_{ki} - f_{ki}^{eq}] \\ IC : f^t \end{array} \right\} \implies f^*, \quad (\text{A.2})$$

$$\left. \begin{array}{l} PDE : \frac{\partial f_{ki}}{\partial t} + v_{kir} \frac{\partial f_{ki}}{\partial r} = 0 \\ IC : f^* \end{array} \right\} \implies f^{**}, \quad (\text{A.3})$$

$$\left. \begin{array}{l} PDE : \frac{\partial f_{ki}}{\partial t} + \frac{1}{r} v_{ki\theta} \frac{\partial f_{ki}}{\partial \theta} = 0 \\ IC : f^{**} \end{array} \right\} \implies f^{t+\Delta t} \quad (\text{A.4})$$

The initial condition for Eq.(A.2) is the initial condition,  $f^t$ , for the complete problem in Eq.(A.1). The solution of Eq.(A.2) after a time  $\Delta t$  is denoted by  $f^*$  and is used as the initial condition for Eq.(A.3). Similarly, the solution of Eq.(A.3)  $f^{**}$  is used as the initial condition for Eq.(A.4). And the solution of Eq.(A.4) is then regarded as an approximation to the solution  $f^{t+\Delta t}$  of the full problem (A.1) at a time  $t + \Delta t$ . Namely,  $f^* = S_{feq}(f^t)$ ,  $f^{**} = S_{fr}(f^*)$ ,  $f^{t+\Delta t} = S_{f\theta}(f^{**})$ . This splitting scheme can be expressed in the succinct form

$$f^{t+\Delta t} = S_{f\theta} S_{fr} S_{feq}(f^t). \quad (\text{A.5})$$

Each numerical sub-problem in Eq.(A.5) is dealt with separately, for a time step  $\Delta t$ . This procedure above is exceedingly simple but is only first order accurate in time, when  $S_{feq}$ ,  $S_{fr}$  and  $S_{f\theta}$  are at least first-order accurate solution operators. A second-order accurate scheme is

$$f^{t+\Delta t} = \begin{cases} S_{f\theta} S_{fr} S_{feq}(f^t) & \text{for } \text{mod}(t, \Delta t) = 0, \\ S_{feq} S_{fr} S_{f\theta}(f^t) & \text{for } \text{mod}(t, \Delta t) = 1, \end{cases} \quad (\text{A.6})$$

where  $S_{feq}$ ,  $S_{fr}$  and  $S_{f\theta}$  are at least second-order accurate solution operators. These can be shown to be second-order accurate every other time step.[33]

Similarly, by introducing solution operators  $S_{\lambda^c}$ ,  $S_{\lambda^r}$  and  $S_{\lambda^\theta}$  for the three subequations in Eq.(30), successively, we can get the following first-order and second-order accurate schemes

$$\lambda^{t+\Delta t} = S_{\lambda^\theta} S_{\lambda^r} S_{\lambda^c}(\lambda^t), \quad (\text{A.7})$$

and

$$\lambda^{t+\Delta t} = \begin{cases} S_{\lambda^\theta} S_{\lambda^r} S_{\lambda^c}(\lambda^t) & \text{for } \text{mod}(t, \Delta t) = 0, \\ S_{\lambda^c} S_{\lambda^r} S_{\lambda^\theta}(\lambda^t) & \text{for } \text{mod}(t, \Delta t) = 1. \end{cases} \quad (\text{A.8})$$

## References

- [1] D. L. Chapman, *Philos. Mag*, 1899, 47(189): 90-104.
- [2] E. J. Jouguet, *Math. Pures Appl*, 1905, 1: 347-425.
- [3] Ya. B. Zeldovich and S. A. Kompaneets, *Zh. Eksp. Teor. Fiz.*, 1940, 10: 542
- [4] J. Von Neumann, *Theory of Detonation Waves*, New York: Macmillan, 1942
- [5] W. Doering, *Ann. Phys.*, 1943, 43: 421-436
- [6] C. Wang, X. Zhang, C. W. Shu, and J. Ning, *J. Comput. Phys.*, 2012, 231(2): 653-665
- [7] J. Sun and J. Zhu, *Theory of Detonation Physics*, Beijing: National Defense Industry Press, 1995 (in Chinese)
- [8] E. L. Lee and C. M. Tarver, *Phys. Fluids*, 1980, 23(12): 2362
- [9] Cochran S. G. , Chan. J. , UCID-18024, (1979)
- [10] J. Cao, *Explosion and Shock Waves*, 1986, 6(2): 137-142 (in Chinese)
- [11] F. Zhao, C. Sun, Y. Wei and J. Chi, *Explosion and Shock Waves*, 1989, 9(4): 338-347 (in Chinese)
- [12] S. Succi, *The Lattice Boltzmann Equation for Fluid Dynamics and Beyond*, Oxford University Press, New York, (2001).
- [13] A. Xu, G. Zhang, Y. Gan, F. Chen, and X. Yu, *Front. Phys.* 7(5), 582 (2012).
- [14] X. Pan, A. Xu, G. Zhang, and S. Jiang, *Int. J. Mod. Phys. C* 18, 1747 (2007).
- [15] Y. Gan, A. Xu, G. Zhang, and Y. Li, *Commun. Theor. Phys.* 50, 201 (2008).
- [16] Y. Gan, A. Xu, G. Zhang, X. Yu, and Y. Li, *Physica A* 387, 1721 (2008).
- [17] Y. Gan, A. Xu, G. Zhang, and Y. Li, *Commun. Theor. Phys.* 56, 490 (2011).
- [18] Y. Gan, A. Xu, G. Zhang, and Y. Li, *Phys. Rev. E* 83, 056704 (2011).
- [19] F. Chen, A. Xu, G. Zhang, Y. Gan, C. Tao, and Y. Li, *Commun. Theor. Phys.* 52, 681 (2009).
- [20] F. Chen, A. Xu, G. Zhang, Y. Li, S. Succi, *EuroPhys. Lett.* 90, 54003 (2010).
- [21] F. Chen, A. Xu, G. Zhang, Y. Li, *Commun. Theor. Phys.* 54, 1121, (2010).
- [22] F. Chen, A. Xu, G. Zhang, Y. Li, *Commun. Theor. Phys.* 55, 325 (2011).
- [23] F. Chen, A. Xu, G. Zhang, Y. Li, *Phys. Lett. A* 375, 2129 (2011).
- [24] F. Chen, A. Xu, G. Zhang, Y. Li, *Commun. Theor. Phys.* 56, 333, (2011).
- [25] F. Chen, A. Xu, G. Zhang, Y. Li, *Theor. & Appl. Mech. Lett.* 1, 052004 (2011).
- [26] B. Yan, A. Xu, G. Zhang, Y. Ying, and H. Li, *Frontiers of Physics*, 8, 94 (2013).
- [27] M. Watari, *Commun. Comput. Phys.* 9, 1293 (2011).
- [28] C. Lin, A. Xu, G. Zhang, Y. Li, S. Succi, e-print arXiv:1302.7104
- [29] Y. Gan, A. Xu, G. Zhang, Y. Yang, arXiv: 1305.4036
- [30] F. Chen, A. Xu, G. Zhang, Y. Wang, arXiv: 1305.4736
- [31] M. Watari and M. Tsutahara, *Phys. Rev. E* 67, 036306 (2003).
- [32] E. F. Toro. *Riemann solvers and numerical methods for fluid dynamics: a practical introduction*[M]. Springer, 2009.
- [33] R. F. Warming, R. M. Beam. *AIAA Journal*, 1976, 14(9): 1241-1249.